



Effects of mantle and subduction-interface rheologies on slab stagnation and trench rollback



Hana Čížková^{a,*}, Craig R. Bina^b

^a Charles University in Prague, Faculty of Mathematics and Physics, Department of Geophysics, Prague, Czech Republic

^b Northwestern University, Department of Earth and Planetary Sciences, Evanston, IL, USA

ARTICLE INFO

Article history:

Received 8 April 2013

Received in revised form 1 August 2013

Accepted 5 August 2013

Available online xxxx

Editor: Y. Ricard

Keywords:

trench rollback

slab stagnation

slab rheology

ABSTRACT

Trench rollback has been a widely discussed phenomenon in recent years, and multiple studies have concentrated on various parameters that may influence trench migration and related aspects of slab deformation in the (upper) mantle. Here we concentrate on the effects of rheological description (yield stress, lower-mantle viscosity, viscosity of crust) in controlling the rollback and associated stagnation of slabs in the transition zone (410–660 km depth). We perform numerical simulations of slab evolution in a 2D Cartesian model with strongly nonlinear rheology combining diffusion creep, dislocation creep and a power-law stress limiter. We demonstrate that trench retreat develops in most models considered, regardless of the subducting plate age or prescribed strength. Rollback then mostly produces slabs that are horizontally deflected at the 660-km phase boundary and remain subhorizontal at the bottom of the transition zone. Slab morphologies are in agreement with stagnant, horizontally deflected structures reported in the transition zone by seismic tomography. Furthermore, if the strength of the slab is limited to less than 0.5 GPa, the slab experiences a significant amount of horizontal buckling. The amplitude of the rollback velocity is sensitive to several model parameters. As one might expect, it increases with the age of the subducting plate, thus reflecting its increasingly negative buoyancy. On the other hand, rollback velocity decreases if we increase the viscosity of the crust and thereby strengthen the coupling between the subducting and overriding plates. High friction on the contact between the subducting and overriding plates may even result in slabs penetrating into the lower mantle after a period of temporary stagnation. Also, reducing the additional negative buoyancy imparted by the 410-km exothermic phase transition suppresses trench rollback. Interpretation of the controls on slab rollback and stagnation may be rather complex in strongly nonlinear rheological models, where, for example, buoyancy effects may be counteracted by associated yield-stress weakening.

© 2013 Elsevier B.V. All rights reserved.

1. Introduction

Subducting slabs may be subject to buckling instabilities upon encountering (both viscous and buoyant) resistance to penetration near 660 km depth. Analysis and modeling of such buckling instabilities (Ribe et al., 2007; Běhounková and Čížková, 2008; Lee and King, 2011) have been performed primarily in the context of buckling in which multiple folds are nearly vertically stacked (i.e., in scenarios featuring minimal slab rollback). Scaling considerations suggest typical buckling amplitudes of ~400 km and periods of ~25 Myr (Lee and King, 2011).

Slab buckling behaviour is complicated by effects of trench retreat (i.e., slab rollback) and trench advance when slabs can lie horizontally at the 660-km interface and their lateral motions make purely vertical buckling improbable. Detailed explo-

ration of parameter spaces (Ribe, 2010; Stegman et al., 2010; Li and Ribe, 2012) yields largely consistent relationships between subduction mode selection (e.g., trench retreat vs. advance) and the two primary governing parameters of viscosity contrast (between upper and lower mantle) and thickness ratio (between upper mantle and subducting slab) – parameters which also relate to the angle at which the leading tip of the subducting slab first encounters the base of the upper mantle. Such work suggests that trench-advance mode is unlikely to be achieved in the Earth, as the viscosity contrast is too low (Ribe, 2010) while the presence of an overriding plate will further inhibit trench advance (Lee and King, 2011).

With the exception of Lee and King (2011), these studies are largely limited to consideration of linear viscosities. They also largely neglect the contributions of mineralogical phase transitions, result in largely vertical stacking or piling of multiple buckles, and generally fail to generate the subhorizontal deflection of slabs at the base of the upper mantle known as slab stagnation (Fukao et al., 2009). Indeed, both mantle phase transitions (Yanagisawa et

* Corresponding author. Tel.: +420 22191 2544; fax: +420 22191 2555.
E-mail address: Hana.Cizkova@mff.cuni.cz (H. Čížková).

al., 2010) and trench retreat (Billen, 2010) have been implicated as significant factors governing slab stagnation (Torii and Yoshioka, 2007).

However, buckling of stagnant slabs – in which multiple buckling episodes result in undulating slabs subhorizontally recumbent along the top of the lower mantle – appeared in some early numerical models (Christensen, 2001) and in interpretive sketches of seismic observations (Schmid et al., 2002). More recently, such behaviour has featured in modeling of trench migration and stagnation (Yoshioka and Naganoda, 2010) and in mineral physical interpretation of seismic velocity anomalies (Zhang et al., 2013). Here we explore (in 2D Cartesian geometry) the time-dependent interplay between trench rollback and buckling in nonlinear composite rheologies, with the inclusion of buoyancy-perturbing mineralogical phase transitions, in a manner that illuminates both buckling and slab stagnation.

Our study of slab deformation in the transition zone focuses primarily upon three aspects of subduction behaviour: slab rollback, slab buckling, and slab stagnation. In assessing the relevant parameter space, we consider the effects of four primary variables: the rheological description of the slab (e.g., yield stress, lower-mantle viscosity), the age of the subducting plate (i.e., initial thermal structure), the viscosity of the crustal layer (i.e., degree of decoupling of subducting and overriding plates), and the Clapeyron slope of the 410-km phase transition (i.e., petrological buoyancy forces).

2. Methods

Our numerical model is based on an incompressible extended Boussinesq approximation of the governing equations without internal heating. The system of equations – including the continuity equation, momentum equation, thermal equation, constitutive relation, and linearised state equation – is solved by the finite-element method using the package SEPRAN (Segal and Praagman, 2005). For a detailed description of the equations and numerical methods, see Čížková et al. (2007). Numerical resolution of the model varies in different parts of the model domain. The finest resolution of 3 km occurs in the uppermost part of the model domain, falling to 8 km in the transition zone, and a relatively coarse resolution of 70 km is sufficient in the lowermost mantle.

We use a composite rheological model (van den Berg et al., 1993) that combines linear diffusion creep, power-law dislocation creep, and a power-law stress limiter approximating Peierls creep (van Hunen et al., 2002). The effective viscosity η_{eff} is calculated from the viscosities of individual creep mechanisms assuming unique stress:

$$\eta_{eff} = \left(\frac{1}{\eta_{diff}} + \frac{1}{\eta_{dist}} + \frac{1}{\eta_y} \right)^{-1}. \quad (1)$$

Here η_{diff} , η_{dist} , and η_y are viscosities of diffusion creep, dislocation creep, and stress limiter respectively:

$$\eta_{diff} = \frac{1}{A_{diff}} \exp\left(\frac{E_{diff} + pV_{diff}}{RT}\right), \quad (2)$$

$$\eta_{dist} = \frac{1}{A_{dist}^{\frac{1}{n}}} e^{(1-n)/n} \exp\left(\frac{E_{dist} + pV_{dist}}{nRT}\right), \quad (3)$$

$$\eta_y = \tau_y e_y^{-1/n_y} e^{1/n_y - 1}. \quad (4)$$

For meaning of symbols, see Table 1.

Our 2D rectangular domain is 10,000 km wide by 2900 km deep (Fig. 1a). The subducting plate stretches from the ridge, positioned in the upper left corner, to the trench, situated in the middle of the upper surface. The initial temperature distribution

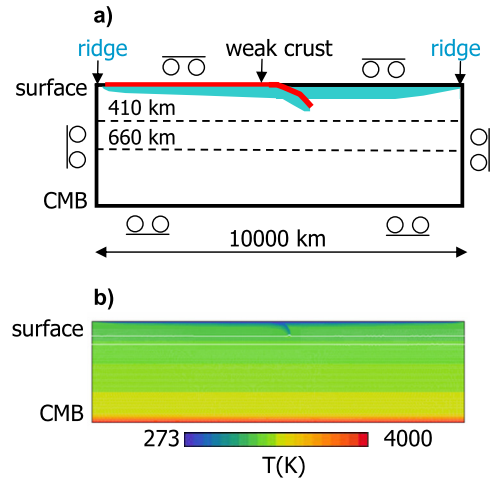


Fig. 1. (a) Schematic sketch of the model domain. Model is 10,000 km wide and 2900 km deep. Dashed lines mark the phase boundaries at 410-km depth and 660-km depth. Subducting and overriding plates are indicated in blue; their thermal age is increasing from their corresponding ridges (upper left and upper right corners) towards the trench in the middle. Red line indicates weak crustal layer prescribed at the top of the subducting plate. (b) Initial temperature distribution with developed slab tip. (For interpretation of the references to colour in this figure legend, the reader is referred to the web version of this article.)

follows a half-space model in the upper part of the model domain, while below the plate the temperature follows an adiabatic profile with a potential temperature of 1573 K. The spreading rate of the ridge varies between 3.33 cm yr^{-1} and 7.0 cm yr^{-1} , thus producing subducting plate ages ranging from 150 to 70 Myr at the trench. An overriding plate starts from a second ridge in the upper right corner, and similarly to the subducting plate its thermal structure follows the half-space model. Its age at the subduction-interface boundary is the same as the age of a corresponding subducting plate. Above the core-mantle boundary a 300-km-wide thermal boundary layer is assumed, with temperature rising from the foot of the adiabat to the CMB temperature of 4000 K. In order to obtain an initial temperature distribution with a tip of the slab already subducted into the mantle, we first execute a short run with a constant velocity prescribed at the top of the subducting plate. When the tip of the slab reaches a depth of 400 km, this kinematic boundary condition is switched off, and the temperature distribution with the developed slab tip is then used as an initial condition (Fig. 1b). The model runs are then executed with impermeable free-slip boundaries. Thermal boundary conditions are of constant temperature at the surface (273 K) and CMB (4000 K), while zero heat flux is prescribed on vertical boundaries. The buoyancy and latent heat effects of the major phase transitions at 410-km depth and 660-km depth are included in the model calculations (Čížková et al., 2007) using a harmonic phase function parameterisation.

On the top of the subducting plate, a 15-km-wide crustal layer is prescribed. Its low viscosity facilitates the decoupling of the two plates (Běhounková and Čížková, 2008). The weak crustal layer is tracked using particle tracers. Below a depth of 200 km, where it is no longer needed to decouple the subducting and overriding plates, it is replaced by mantle material for numerical convenience. No additional density contrast is associated with this crustal layer.

The activation parameters as well as rheological prefactors vary between the upper and the lower mantle. In the upper mantle and transition zone we assume activation parameters based on Hirth and Kohlstedt (2003). In the lower mantle, dislocation creep is usually not considered to play an important role (Karato et al., 1995); we therefore assume only diffusion creep deformation there. Diffusion creep parameters that predict the sinking speeds

Table 1
Symbols and model parameters.

| Symbol | Meaning | Value | Units |
|---|---|---|----------------------------------|
| Upper mantle and transition zone rheology | | | |
| A_{diff} | Pre-exponential parameter of diffusion creep ^a | 1×10^{-9} | $\text{Pa}^{-1} \text{s}^{-1}$ |
| A_{disl} | Pre-exponential parameter of dislocation creep ^a | 3.1×10^{-17} | $\text{Pa}^{-n} \text{s}^{-1}$ |
| E_{diff} | Activation energy of diffusion creep ^a | 3.35×10^5 | J mol^{-1} |
| E_{disl} | Activation energy of dislocation creep ^a | 4.8×10^5 | J mol^{-1} |
| V_{diff} | Activation volume of diffusion creep ^a | 4.0×10^{-6} | $\text{m}^3 \text{mol}^{-1}$ |
| V_{disl} | Activation volume of dislocation creep ^a | 11×10^{-6} | $\text{m}^3 \text{mol}^{-1}$ |
| n | Power-law exponent | 3.5 | – |
| η_{crust} | Viscosity of crust | $10^{19}–10^{21}$ | Pa s |
| τ_y | Yield stress | $2 \times 10^8–10^9$ | Pa |
| e_y | Reference strainrate | 1×10^{-15} | s^{-1} |
| n_y | Stress limiter exponent | 10 | – |
| p | Hydrostatic pressure | – | Pa |
| R | Gas constant | 8.314 | $\text{JK}^{-1} \text{mol}^{-1}$ |
| T | Temperature | – | K |
| e | Second invariant of the strainrate | – | s^{-1} |
| Lower-mantle rheology | | | |
| A_{diff} | Pre-exponential parameter of diffusion creep | $1.3 \times 10^{-17}–1.3 \times 10^{-16}$ | $\text{Pa}^{-1} \text{s}^{-1}$ |
| E_{diff} | Activation energy of diffusion creep ^b | 2×10^5 | J mol^{-1} |
| V_{diff} | Activation volume of diffusion creep ^b | 1.1×10^{-6} | $\text{m}^3 \text{mol}^{-1}$ |
| Other model parameters | | | |
| κ | Diffusivity | 10^{-6} | $\text{m}^2 \text{s}^{-1}$ |
| G | Gravitational acceleration | 9.8 | m s^{-2} |
| ρ_0 | Reference density | 3416 | kg m^{-3} |
| c_p | Specific heat | 1250 | $\text{J kg}^{-1} \text{K}^{-1}$ |
| α_0 | Surface thermal expansivity | 3×10^{-5} | K^{-1} |
| γ_{410} | Clapeyron slope 410 km phase transition ^c | $1–4 \times 10^6$ | Pa K^{-1} |
| γ_{660} | Clapeyron slope 660 km phase transition ^c | $–2.5 \times 10^6$ | Pa K^{-1} |
| $\delta\rho_{410}$ | Density contrast 410 km phase transition ^d | 273 | kg m^{-3} |
| $\delta\rho_{660}$ | Density contrast 660 km phase transition ^d | 341 | kg m^{-3} |

^a Parameters of wet olivine after [Hirth and Kohlstedt \(2003\)](#).

^b Lower-mantle activation parameters of family A models by [Čížková et al. \(2012\)](#).

^c [Bina and Helffrich \(1994\)](#).

^d [Steinbach and Yuen \(1995\)](#).

of detached slabs in the lower mantle as reported by [van der Meer et al. \(2010\)](#) are adopted here ([Čížková et al., 2012](#)). Our assumed thermal expansivity varies with depth from $3 \times 10^{-5} \text{ K}^{-1}$ at the surface to $\sim 1 \times 10^{-5} \text{ K}^{-1}$ at the core-mantle boundary ([Chopelas and Boehler, 1992](#); [Katsura et al., 2009](#)).

As several model parameters that may potentially influence slab dynamics are not particularly well constrained, we perform here a parametric study in which we vary some of these parameters. As already mentioned above, the age of both plates at the trench is assumed to vary between 70 Myr and 150 Myr. The older and colder plates are not only more negatively buoyant than the younger ones, but they are also stiffer due to the temperature dependence of viscosity (Eqs. (2), (3)). Lower-mantle viscosity influences the resistance of the lower mantle to slab penetration ([Loiselet et al., 2010](#)). We therefore vary here the diffusion creep prefactor in the lower mantle and thus generate three profiles of lower-mantle viscosity: (i) a reference profile based on the analysis of slab sinking speed ([Čížková et al., 2012](#)) where viscosity increases by a factor of 7 at the 660-km phase interface, (ii) a profile with lower-mantle viscosity twice the value of the reference profile, and (iii) a profile with the lower mantle ten times stiffer than in the reference profile (see supplementary Fig. 1). Further, potential rollback should be influenced by the strength of the decoupling crustal layer. We test this effect by varying crustal viscosity in the range $10^{19} \text{ Pa s}–10^{21} \text{ Pa s}$. Another parameter that controls slab deformation is the yield stress of the stress-limiting mechanism. We take a reference value of 0.5 GPa here, which should correspond to the yield strength of olivine at about 900 °C ([Billen, 2010](#)), and we also test both a lower value of 0.2 GPa and a higher yield stress of 1 GPa. Finally, it has been shown by [Běhounková and Čížková \(2008\)](#) that the buckling behaviour of the slab is controlled primar-

ily by the buoyancy associated with the 410-km phase transition. We therefore test here the effect of this phase change by varying its Clapeyron slope between 1 MPa K^{-1} and 4 MPa K^{-1} . Results of the individual model runs will be discussed with respect to the reference-state model defined as follows: A-family viscosity profile of [Čížková et al. \(2012\)](#), yield stress 0.5 GPa, plate age at the trench 100 Myr, viscosity of the crustal layer 10^{20} Pa s , and Clapeyron slope of the 410-km phase transition 3 MPa K^{-1} .

3. Results

Time evolution of the subducting slab in the reference model case is illustrated in [Fig. 2](#). Panel 2a shows six snapshots of the temperature field in the upper central part of the model domain. In the initial state the tip of the slab just reaches the 410-km phase transition. Due to the additional negative buoyancy associated with this exothermic phase change (cf. [Fig. 7c](#)), the slab accelerates, and its plate velocity reaches a maximum of about 16 cm yr^{-1} . This is reflected in the first peak of the plate velocity plotted as a function of time ([Fig. 2b](#), blue curve). As the slab tip arrives at the base of the transition zone, it slows down due to the combined resistance of the endothermic phase transition at 660-km depth and an associated increase in viscosity. The slab then deflects horizontally and remains trapped in the transition zone. Quasiperiodic horizontal buckling is observed while the slab is rolling back, with rollback velocity maxima occurring at plate velocity minima and vice versa ([Fig. 2b](#)). The dominant period of plate velocity oscillations is about 20 Myr as illustrated in [Fig. 2c](#), where the spectra of plate and rollback velocities are displayed (windowed at 5–100 Ma to exclude the first velocity peak imposed by the initial conditions). Slab dip angle shows similar oscillatory behaviour as plate and rollback

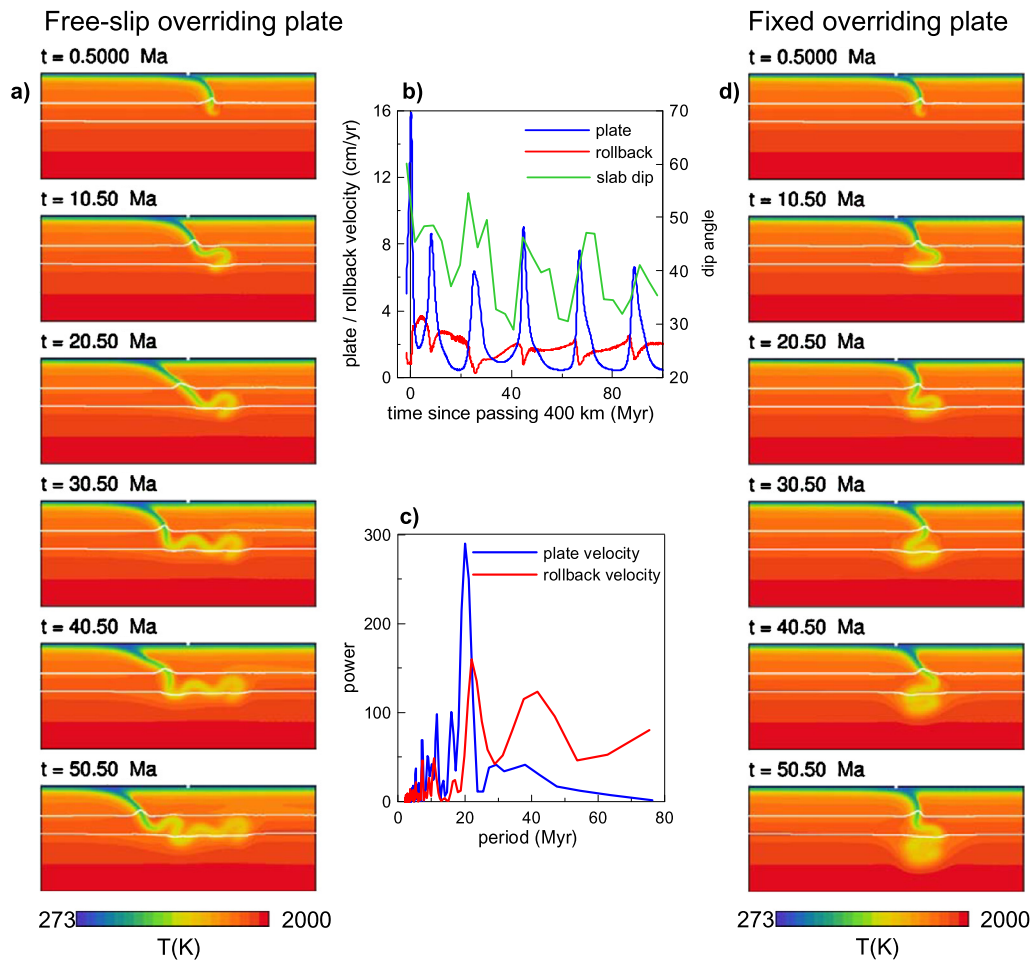


Fig. 2. Time evolution of the subducting plate. (a) Six snapshots of temperature illustrating the descent of the plate in the reference model. Only a part of the model domain 1450 km deep and 3700 km wide is shown. White lines indicate positions of the major mantle phase transitions at 410-km and 660-km depths. White squares in the topmost part of the overriding plate show the initial position of the trench. Time of the snapshots is measured from the moment when the slab tip crosses 400-km depth. (b) Plate (blue) and rollback (red) velocities and slab dip angle (green) in the reference model as a function of time. (c) Spectra of plate (blue) and rollback (red) velocities (windowed at 5–100 Ma to exclude first velocity peak imposed by initial conditions) in the reference model. (d) The same as (a), but for the model where rollback was inhibited by no-slip boundary condition at the surface of the overriding plate. (For interpretation of the references to colour in this figure legend, the reader is referred to the web version of this article.)

velocities (Fig. 2b, green line). During periods of high plate velocities the slab is dipping at steep angles ($\sim 50^\circ$), while high rollback velocities are associated with shallower dip angles ($\sim 30^\circ$). Sub-horizontal deformation of the slab in the transition zone is directly linked to slab rollback. If the subducting plate could not roll back, the slab would penetrate into the lower mantle and fold vertically. This is demonstrated in Fig. 2d, where the time evolution of temperature is shown for a model with a fixed overriding plate (ensured by a no-slip boundary condition along the surface of the overriding plate).

Let us now look more closely at the process of subhorizontal buckling occurring in the reference model case with rollback. Fig. 3 shows six snapshots of viscosity distribution in the zoomed images that illustrate formation of the first two horizontal buckles. The following general outline of the dynamics can be gleaned from detailed examination of time-varying 2D plots of temperature, viscosity, strain rate, stress invariants, and velocity components. The slab descends at some initial dip angle ($< 90^\circ$) due to its negative thermal buoyancy, in largely free motion. The slab is largely in down-dip extension, especially along its upper surface where it is subject to bending moments. (The overriding plate is in compression, due to ridge-push force opposed at the subduction interface.) As the slab encounters the (thermally uplifted) wadsleyite-forming phase boundary near 410 km, it accelerates due to the additional

negative petrological buoyancy acquired upon its transformation to denser phases at shallower depths than in the surrounding mantle. The consequently enhanced bending moment begins to weaken the slab through increased strain rates. This regime is marked by high plate velocities and low rollback velocities (Fig. 3a). Eventually the slab encounters significant resistance near 660 km, due to both the viscosity increase and the positive buoyancy associated with the (thermally depressed) perovskite-forming phase boundary. As a result, the slab decelerates, and down-dip compressional stresses are transmitted up the slab. However, shallower portions of the slab are still subject to negative thermal (and, slightly deeper, petrological) buoyancy. Because the dip is not vertical, these shallow portions of the slab are not fully supported by the 660-km resistance below, and they can begin to descend vertically without undue resistance, thereby rolling back the slab and inducing trench retreat. (The overriding plate follows, due to ridge-push as it slides downhill along its age-dependent base.) This results in buckling of the slab, which is facilitated by weakening of the slab at the fold hinge due to high strain rates. This regime is marked by low plate velocities and high rollback velocities (Fig. 3b). Once such a buckle has formed, the seaward portion of the slab resumes largely free descent, returning to the regime marked by high plate velocities and low rollback velocities. The buckle folds more tightly, facilitated by strain-rate weakening, as the seaward portion of the slab

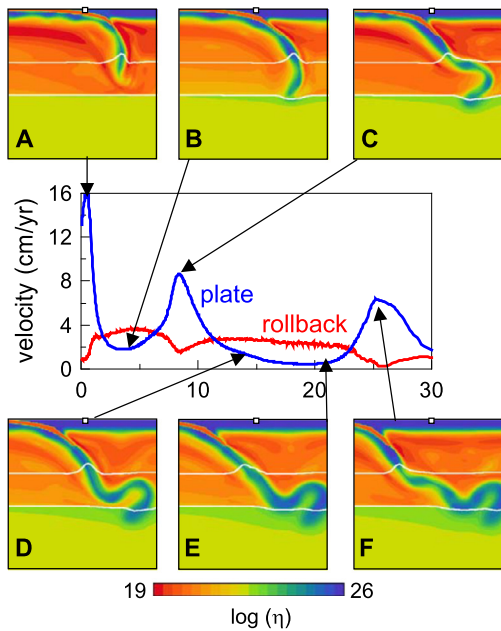


Fig. 3. Detail of slab deformation in the first 25 Myr in the reference model. Middle panel shows plate (blue line) and rollback (red line) velocities as functions of time (cf. Fig. 2b). Six snapshots of effective viscosity are shown at six moments indicated by arrows on velocity plot. Only a part of the model domain, 1150 km deep and 1150 km wide, is shown. White lines indicate positions of major mantle phase transitions; white square in the topmost part of the overriding plate indicates initial position of the trench. (For interpretation of the references to colour in this figure legend, the reader is referred to the web version of this article.)

descends while the trenchward portion remains largely supported by 660-km resistance (Fig. 3c). This process continues, with the seaward portion accelerating through the (uplifted) 410-km transition, until it encounters the (depressed) 660-km resistance. At this point, the slab returns to the regime marked by low plate velocities and high rollback velocities (Fig. 3d, e). Such oscillating behaviour results in a subhorizontal distribution of buckle folds along the base of the mantle transition zone (Fig. 3f). Clearly, the falling depth (~660 km) to resistance must partially govern the period of the resulting oscillations between regimes.

The effect of the lower-mantle viscosity is demonstrated in Fig. 4, where a snapshot of viscosity taken after 80 Myr evolution from the initial state is shown for three model cases. Panel 4a is for the reference model case; panel 4b is for a model with a doubled lower-mantle viscosity, and panel 4c is for a model with lower-mantle viscosity increased by one order of magnitude relative to the reference model (supplementary Fig. 1). Increasing the stiffness of the lower mantle impedes the flow in the upper mantle and transition zone and thus decreases both plate and rollback velocities. Moreover, higher lower-mantle viscosities change also the periodicity of buckling – where the period is about 25 Myr in the case of a twice stiffer lower mantle, while an order of magnitude increase of lower-mantle viscosity with respect to the reference model results in periods of almost 40 Myr.

Further, we evaluate the role of the crustal strength. The results are summarised in Fig. 5, where one snapshot of viscosity is shown for five models with successively increasing crustal strength. Models with weak crust (10^{19} – 2×10^{20} Pa s) are characterised by subhorizontal deformation above the 660-km interface, and slabs remain trapped in the transition zone. Both plate and rollback velocities decrease with increasing crustal viscosity as does the frequency of buckling. Stiffer crust (5×10^{20} – 10^{21} Pa s) further reduces the plate and rollback velocities, and slabs now can penetrate the endothermic phase boundary and reach the lower mantle. A primary effect of a stiffer crustal layer along the subduction

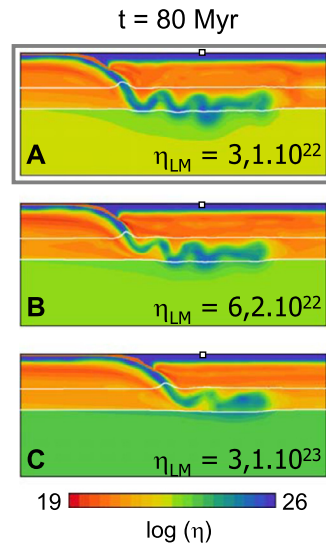


Fig. 4. One snapshot of effective viscosity taken after 80 Myr evolution for three models with different lower-mantle viscosities. Part of the model domain, 1450 km deep and 3700 km wide, is shown. White lines mark the positions of major mantle phase transitions; white square indicates initial position of the trench. Grey frame (panel A) indicates reference model discussed in Fig. 2a. Panel B is for the model with lower-mantle viscosity twice that in the reference model; panel C is for model with ten times higher lower-mantle viscosity than in the reference model. Volume-averaged lower-mantle viscosities are indicated in lower left corner of each panel.

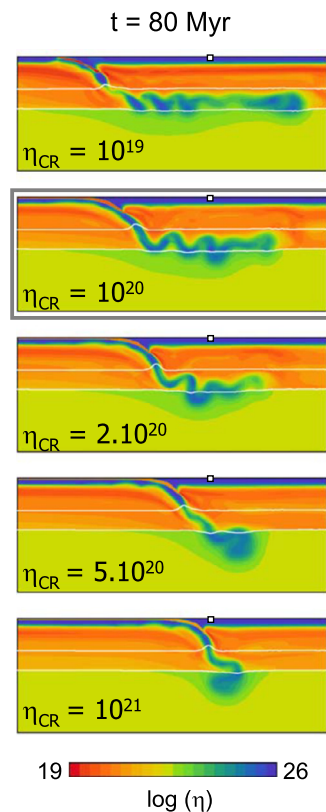


Fig. 5. One snapshot of effective viscosity taken after 80 Myr evolution for five models with different crustal strengths. Grey frame indicates the reference model discussed in detail in Fig. 2a. Part of the model domain, 1450 km deep and 3700 km wide, is shown. White lines mark the position of major mantle phase transitions; white square indicates initial position of the trench. Viscosity of the weak crust is given in lower left corner of each panel.

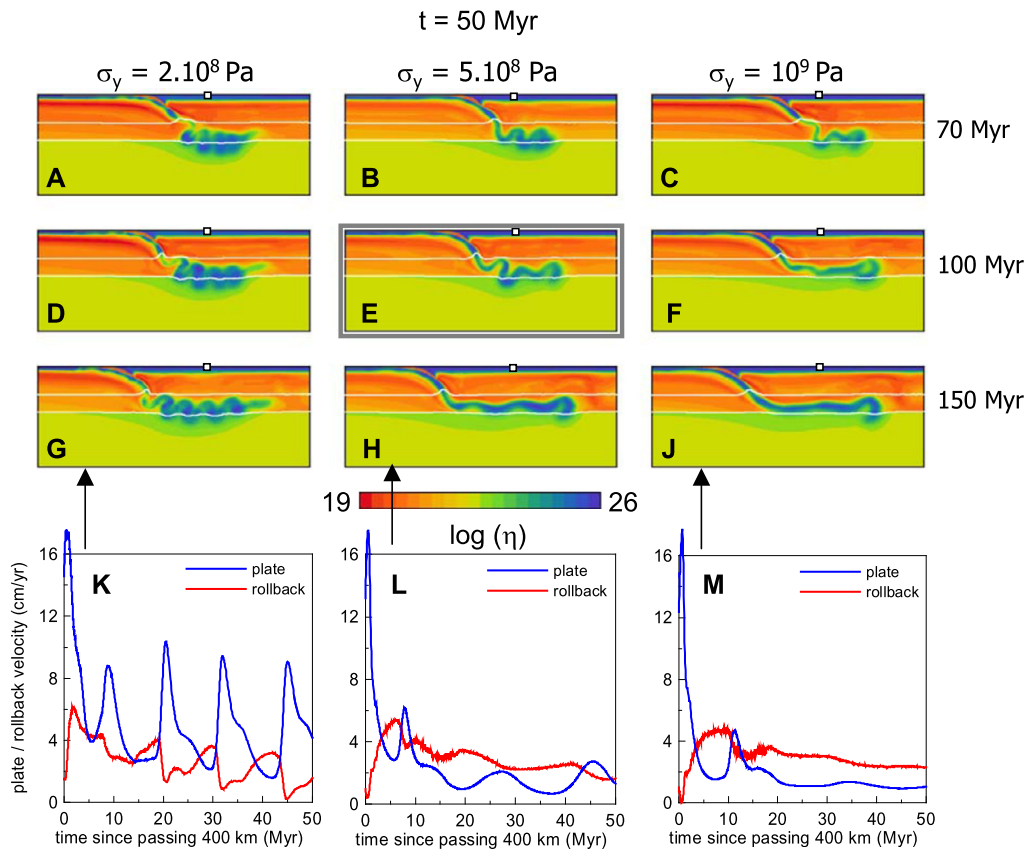


Fig. 6. One snapshot of effective viscosity taken after 50 Myr evolution for nine models with varying yield stress and varying plate age. Grey frame indicates the reference model discussed in detail in Fig. 2a. Part of the model domain, 1450 km deep and 3900 km wide, is shown. White lines mark the position of major mantle phase transitions; white square indicates initial position of the trench. First row of panels is for models with plate age of 70 Myr; second row is for plate age of 100 Myr, and third row is for models with plate age of 150 Myr. First column of panels is for yield stress 0.2 GPa, second column for yield stress 0.5 GPa, and third column for yield strength 1 GPa. Fourth row (panels K, L, M) shows the plate (blue line) and rollback (red line) velocities as a function of time for models with plate age of 150 Myr. Arrows indicate corresponding models. (For interpretation of the references to colour in this figure legend, the reader is referred to the web version of this article.)

interface is to inhibit the largely free descent of the slab. As the deeper portions of the slab are still subject to negative buoyancy, resistance at the shallower interface imposes a bending moment which rotates the slab to a steeper dip angle ($\approx 90^\circ$). As the slab now descends nearly vertically, its response to encountering resistance near 660 km is different. The shallower portions of the slab still subject to negative buoyancy cannot continue to descend freely. Buckling can only occur in a nearly vertical mode, inducing only minimal rollback. The period of buckles increases from about 15 Myr in case of a weak crust (10^{19} Pa s) to about 35 Myr in case of the strongest crust considered (10^{21} Pa s).

So far we have discussed the results obtained with a slab 100 Myr old with a reference yield stress of 0.5 GPa. Fig. 6 illustrates the effects of varying plate age at the trench and varying yield stress on one snapshot of viscosity ($t = 50$ Myr after initial state). Each column is for one value of yield stress, and each row is for one plate age. The middle panel 6e is for the reference model that was discussed in detail in Fig. 2. As expected, older and thus more negatively buoyant slabs exhibit faster rollback. The amount of horizontal buckling experienced by the slab is controlled by its age, which determines the strength through thermal dependence of viscosity. While the young slab (70 Myr old) is always buckled (Fig. 6a–c), the old and stiff slab (150 Myr old, yield stress 1 GPa – Fig. 6j) is lying flat at the 660-km discontinuity. The period of horizontal buckles is increasing with increasing plate strength (stiffness) as illustrated in panels 6k–m, where plate and rollback velocities are plotted for three models with plate age 150 Myr. A weak slab (yield stress 0.2 GPa – Fig. 6k) shows peri-

odic plate velocity with period ~ 10 Myr and peak maxima about 10 cm yr^{-1} . A stronger slab (yield stress 0.5 GPa – Fig. 6l) also shows periodic buckling, but its period is longer (~ 20 Myr) and peak values much lower ($2\text{--}3 \text{ cm yr}^{-1}$). The strongest slab considered (yield stress 1 GPa – Fig. 6m) forms only one buckle (plate velocity maximum at ~ 10 Myr). Later the plate velocity remains low (less than 2 cm yr^{-1}) with only a very mild increase at about 35 Myr. Rollback velocity in the case of the weakest slab (Fig. 6k) has minima occurring at plate velocity maxima, similarly to the reference model case (cf. Fig. 2b). If stronger slabs are considered (Fig. 6l, m), this feature is much less prominent. Average rollback velocity, however, is similar in all models with the same plate age.

As the slab weakening that determines deformation is to a certain extent controlled by the extra negative buoyancy exerted by an exothermic phase change at 410-km depth, we finally study the effect of its Clapeyron slope. Results are summarised in Fig. 7a, where one snapshot of viscosity is shown for models with Clapeyron slope varying between 1 MPa K^{-1} and 4 MPa K^{-1} . The reference model discussed in Fig. 2 has a Clapeyron slope of 3 MPa K^{-1} (Fig. 7a, grey frame). Clapeyron curves that illustrate the elevation of a 410-km phase interface are given in Fig. 7b, and the additional density anomaly associated with the elevated phase boundary is shown in Fig. 7c. A primary effect of a smaller effective Clapeyron slope at the wadsleyite-forming boundary is to decrease the acceleration experienced by the slab as it descends past 410 km. This decrease in the petrological buoyancy contribution results in shallower dip angles as well as smaller stresses and lower strain rates (thus dampening the extent of weakening of the slab), thereby

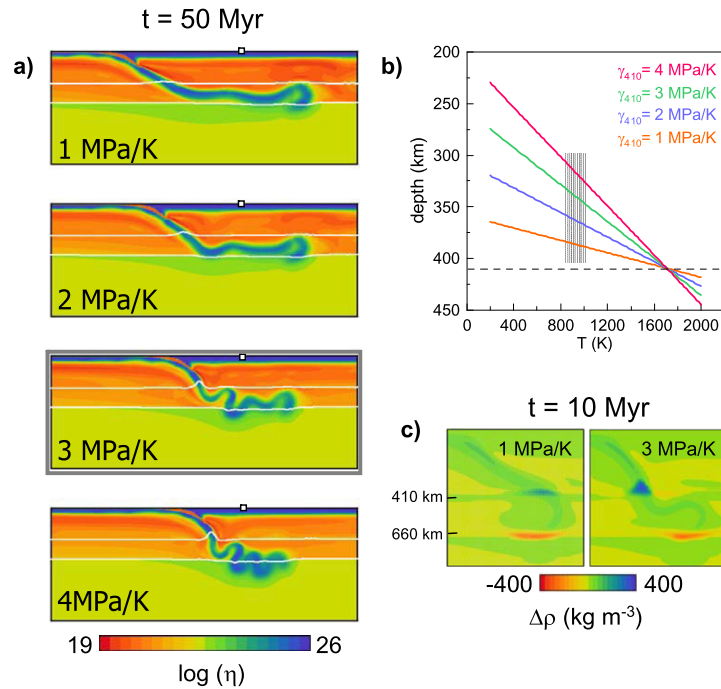


Fig. 7. (a) One snapshot of effective viscosity taken after 50 Myr evolution for nine models with varying Clapeyron slope of the 410-km phase change. Grey frame indicates the reference model discussed in detail in Fig. 2a. Part of the model domain, 1450 km deep and 3900 km wide, is shown. White lines mark the position of major mantle phase transitions; white square indicates initial position of the trench. Clapeyron slope of each model is indicated in the lower left corner of a corresponding panel. (b) Clapeyron curves of 410-km phase transition in depth–temperature space. Grey area depicts typical slab temperature minima in a depth range 300–400 km. Dashed line marks the position of 410-km interface. (c) Density anomalies (with respect to horizontally averaged density) in a zoomed window located around subducting slab for models with $\gamma_{410} = 1 \text{ MPa K}^{-1}$ and $\gamma_{410} = 3 \text{ MPa K}^{-1}$ (reference model). Snapshot is taken at 10 Myr. (For interpretation of the references to colour in this figure legend, the reader is referred to the web version of this article.)

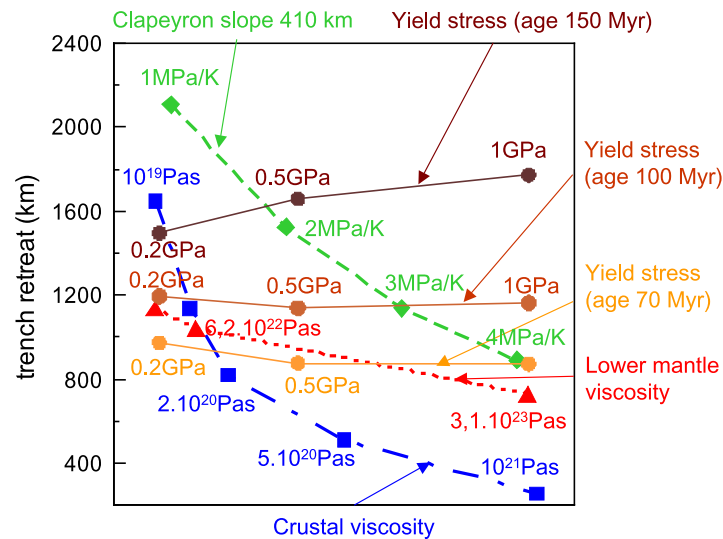


Fig. 8. Trench retreat as a function of all parameters tested in this study. Vertical axis shows the distance travelled by the trench in 60 Myr. Green diamonds: Clapeyron slope varying in the range 1 MPa K^{-1} – 4 Pa K^{-1} ; blue squares: crustal viscosity varying in the range 10^{19} Pa s – 10^{21} Pa s ; red triangles: lower-mantle viscosity varying in the range $3.1 \times 10^{22} \text{ Pa s}$ – $3.1 \times 10^{23} \text{ Pa s}$; dark brown dots: yield stress varying between 0.2 GPa and 1 GPa with plate age 150 Myr; light brown dots: yield stress varying between 0.2 GPa and 1 GPa with plate age 100 Myr; yellow dots: yield stress varying between 0.2 GPa and 1 GPa with plate age 70 Myr. (For interpretation of the references to colour in this figure legend, the reader is referred to the web version of this article.)

leading to less tightly folded buckles. A very low Clapeyron slope of 1 MPa K^{-1} thus results in a flat-lying slab and fast rollback, while an extremely high Clapeyron slope of 4 MPa K^{-1} produces a tightly folded subhorizontal slab with more than twice slower rollback. Variations in the Clapeyron slope of the 410-km phase interface control the strength of the slab through stress-dependent rheology – in that slab weakening associated with higher values of Clapeyron slope is necessary to produce subhorizontal buckling.

This is in agreement with the results of Běhouňková and Čížková (2008), who have shown that the weakening effect of the 410-km incremental negative buoyancy is necessary to produce vertical folding. The effect of the 410-km phase transition may, however, not be an essential ingredient of the model, if the assumed rheological description generally produces weaker slabs (Ribe et al., 2007).

4. Discussion and conclusions

Results obtained in this study are summarised in Fig. 8. Here total trench retreat, that is the distance travelled by the trench, within 60 Myr of model evolution is plotted as a function of different model parameters. Among the model parameters tested, the strongest control on trench retreat is exercised by the crustal viscosity. Increased friction on the contact between the subducting and overriding plates facilitates steeper dip angles and thus reduces rollback. Increasing the stiffness of the crustal layer by two orders of magnitude reduces the total trench retreat by 1400 km. Similarly strong is the effect of the Clapeyron slope of the exothermic phase transition at 410-km depth. If it is relatively high, the associated additional negative buoyancy produces high strain rates and weakens the slab through the nonlinear strain-rate dependent rheology, thus facilitating buckling and generally increasing plate velocities while decreasing rollback velocities. A low Clapeyron slope, on the other hand, produces stronger slabs that subduct at shallower dip angles and experience faster rollback. Increasing the Clapeyron slope from 1 MPaK^{-1} to 4 MPaK^{-1} reduces the total trench retreat by 1200 km. The effect of lower-mantle viscosity is much less pronounced than the previous two factors. Increasing the lower-mantle viscosity by a factor of ten with respect to the reference profile decreases both plate and rollback velocities and reduces the total trench retreat by 400 km. The effect of yield strength is yet smaller. In the case of younger slabs (70 Myr and 100 Myr), it is essentially negligible. In the case of the oldest slab (150 Myr), the trench retreat is greater by about 270 km for the strongest slab (yield stress 1 GPa) as strain-rate induced weakening is less effective here. Finally, increasing the age of the subducting plate enhances rollback – the difference between the oldest and youngest slabs could account for as much as a 900 km increase in the total trench retreat.

Among other observations, we find that subhorizontal buckling (as opposed to purely vertical stacking) is primarily observed, so that trench rollback usually results in a stagnant-slab situation in the transition zone. Here a mobile (as opposed to fixed) overriding plate plays an important role in allowing such horizontal buckling. We have also demonstrated the importance of a weak crustal layer in governing trench retreat. The lubricating nature of such a weak crustal layer has already been suggested to contribute to asymmetric subduction (Crameri et al., 2012), and physically it may arise from the presence of low-viscosity foliated serpentine (Hilaret et al., 2007; Amiguet et al., 2012). Higher crustal viscosities reduce both plate and rollback velocities, eventually yielding a partially penetrative (rather than stagnant) slab.

Overall, rollback velocities are generally smaller than plate velocities. Larger lower-mantle viscosities result in reduction of both plate and rollback velocities. Older, heavier plates exhibit faster rollback. Indeed, old, cold slabs which are too strong to easily buckle exhibit faster rollback than weaker slabs showing horizontal buckling. Both plate and rollback velocities generally exhibit oscillatory behaviour that reflects slab buckling. Dominant periods in the reference model are of order 20 Myr, in agreement with prior scaling analyses (Lee and King, 2011). Periods of the velocity oscillations are associated with the wavelengths of the folds of the plate (Schmalholz et al., 2002) that in turn are sensitive to the stiffness of the subducting slab. Therefore, the periods of velocity oscillations vary between 15 and 35 Myr in our models, depending on yield stress, lower-mantle viscosity and crustal viscosity.

Lower values of the Clapeyron slope associated with the wadsleyite-forming phase transition near 410 km depth serve to suppress yield-stress weakening and buckling, thereby yielding faster rollback. Careful observation of the time evolution of the shape of the thermally uplifted 410-km discontinuity in the slab (e.g., Fig. 3a, e) reveals a temporal oscillation in morphol-

ogy – which we call a “*píd’alka*” or “inchworm” mode, as it resembles the locomotion of *Geometridae* moth larvae – that is synchronised to corresponding oscillations in slab and rollback velocities. These oscillations are also reflected in slab dip-angle variations that may further influence, for example, the exhumation of high-pressure metamorphic rocks (Brun and Faccenna, 2008; Husson et al., 2009).

Trench advance is rarely observed in our models, although rates of trench retreat drop nearly to zero for very stiff values of crustal viscosity. That is not very surprising in light of some previous studies. Stegman et al. (2010) predict trench advance in regimes featuring very strong slabs while our model rheologies include slab weakening, so that we are unlikely to attain to their conditions favouring trench advance (which they themselves suggest do not correspond to any conditions on Earth at present). Tendency toward trench advance is also limited by the relatively low viscosity increase (order $10\text{--}10^2$) near 660 km (Ribe, 2010). Moreover, the overriding plate may play an important role here. As shown by Yamato et al. (2009), the presence of a stiff overriding plate decreases trench retreat. A strong overriding plate that is hard to deform also hinders trench advance. Trench advance is further inhibited by the ridge-push of the overriding plate; in order to suppress rollback or to obtain trench advance, pull would have to be exerted on the overriding plate (Chertova et al., 2012) rather than simply the push arising from gravitational sliding of the ageing upper plate.

Our modeling study shows the effects of various parameters on the dynamics and resulting morphology of the subducting slabs. A natural question arises, whether our results could be correlated with the slab morphologies imaged by seismic tomography. A straightforward comparison is however not simple. As we don’t clearly know how the yield stress might vary across subduction zones, and it seems unlikely that either the lower-mantle viscosity or the wadsleyite-forming Clapeyron slope should vary across subduction zones, the variations in crustal viscosity are left as a possible significant variable. All else being equal, weaker crustal layers should lead to greater trench retreat and flat-lying slab. A possible factor governing crustal strength could be weakening by serpentinisation (Hilaret et al., 2007; Amiguet et al., 2012). More heavily serpentinised crust in the interfacial coupling zone would be weaker, and slabs with larger thermal parameters (older, colder, faster) would likely retain more serpentine to great depths. However, several factors suggest instead a common depth of slab-mantle decoupling (Wada and Wang, 2009) across subduction zones. This is clearly an area where much interesting work remains to be done. A detailed analysis of the terrestrial observations that would be needed for comparison with our modeling results is, however, beyond the scope of the present paper.

Acknowledgements

We thank Scott King and Philippe Yamato for constructive and valuable comments that helped to improve the manuscript. This research was supported by the Czech Science Foundation Grant P210/11/1366 and by the research project MSM0021620860. C.R.B. is grateful to Charles University in Prague for support as a visiting researcher.

Appendix A. Supplementary material

Supplementary material related to this article can be found online at <http://dx.doi.org/10.1016/j.epsl.2013.08.011>.

References

- Amiguet, E., Reynard, B., Caracas, R., Van de Moortèle, B., Hilairt, N., Wang, Y., 2012. Creep of phyllosilicates at the onset of plate tectonics. *Earth Planet. Sci. Lett.* 345–348, 142–150.
- Běhouňková, M., Čížková, H., 2008. Long-wavelength character of subducted slabs in the lower mantle. *Earth Planet. Sci. Lett.* 275, 43–53.
- Billen, M., 2010. Slab dynamics in the transition zone. *Phys. Earth Planet. Inter.* 183, 296–308.
- Bina, C., Helffrich, G., 1994. Phase transition Clapeyron slopes and transition zone seismic discontinuity topography. *J. Geophys. Res.* 103, 15853–15860.
- Brun, J.P., Faccenna, C., 2008. Exhumation of high-pressure rocks driven by slab rollback. *Earth Planet. Sci. Lett.* 272, 1–7.
- Chertova, M., Geenen, T., van den Berg, A., Spakman, W., 2012. Using open sidewalls for modelling self-consistent lithosphere subduction dynamics. *Solid Earth* 3, 313–326.
- Chopelas, A., Boehler, R., 1992. Thermal expansivity in the lower mantle. *Geophys. Res. Lett.* 19, 1983–1986.
- Christensen, U.R., 2001. Geodynamic models of deep subduction. *Phys. Earth Planet. Inter.* 127, 25–34.
- Čížková, H., van Hunen, J., van den Berg, A.P., 2007. Stress distribution within subducting slabs and their deformation in the transition zone. *Phys. Earth Planet. Inter.* 161, 202–214.
- Čížková, H., van den Berg, A.P., Spakman, W., Matyska, C., 2012. The viscosity of Earth's lower mantle inferred from sinking speed of subducted lithosphere. *Phys. Earth Planet. Inter.* 200–201, 56–62.
- Cramer, F., Tackley, P.J., Meilick, I., Gerya, T.V., Kaus, B.J.P., 2012. A free plate surface and weak oceanic crust produce single-sided subduction on Earth. *Geophys. Res. Lett.* 39, L03306.
- Fukao, Y., Obayashi, M., Nakakuki, T., 2009. Stagnant slab: A review and the Deep Slab Project Group. *Annu. Rev. Earth Planet. Sci.* 37, 19–46.
- Hilairt, N., Reynard, B., Wang, Y., Daniel, I., Merkel, S., Nishiyama, N., Petitgirard, S., 2007. High-pressure creep of serpentine, interseismic deformation, and initiation of subduction. *Science* 318, 1910–1913.
- Hirth, G., Kohlstedt, D., 2003. Rheology of the upper mantle and mantle wedge: A view from the experimentalists. In: *Inside the Subduction Factory*. In: *Geophysics Monogr.*, vol. 138. American Geophysical Union, Washington, DC.
- Husson, L., Brun, J.P., Yamato, P., Faccenna, C., 2009. Episodic slab rollback fosters exhumation of HP-UHP rocks. *Geophys. J. Int.* 179, 1292–1300.
- Karato, S.-I., Zhang, S., Wenk, H.R., 1995. Superplasticity in Earth's lower mantle: Evidence from seismic anisotropy and rock physics. *Science* 20, 458–461.
- Katsura, T., Yokoshi, S., Kawabe, K., Shatskiy, A., Manthilake, M.A.G.M., Zhai, S., Fukui, H., Hegoda, H.A.C.I., Yoshino, T., Yamazaki, D., Matsuzaki, T., Yoneda, A., Ito, E., Sugita, M., Tomioka, N., Hagiya, K., Nozawa, A., Funakoshi, K., 2009. P-V-T relations of MgSiO₃ perovskite determined by in situ X-ray diffraction using a large-volume high-pressure apparatus. *Geophys. Res. Lett.* 36, L01305.
- Lee, C., King, S.D., 2011. Dynamic buckling of subducting slabs reconciles geological and geophysical observations. *Earth Planet. Sci. Lett.* 312, 360–370.
- Li, Z.-H., Ribe, N.M., 2012. Dynamics of free subduction from 3-D boundary element modeling. *J. Geophys. Res.* 117, B06408.
- Loiselet, C., Braun, J., Husson, L., Le Carlier de Veslud, C., Thieulot, C., Yamato, P., Grujic, D., 2010. Subducting slabs: Jellyfishes in the Earth's mantle. *Geochem. Geophys. Geosyst.* 11, <http://dx.doi.org/10.1029/2010GC003172>, Q08016.
- Ribe, N.M., 2010. Bending mechanics and mode selection in free subduction: A thin-sheet analysis. *Geophys. J. Int.* 180, 559–576.
- Ribe, N.M., Stutzmann, E., Ren, Y., van der Hilst, R., 2007. Buckling instabilities of subducted lithosphere beneath the transition zone. *Earth Planet. Sci. Lett.* 254, 173–179.
- Schmalholz, S.M., Podlatchikov, Y., Burg, J.P., 2002. Control of folding by gravity and matrix thickness: Implications for large-scale folding. *J. Geophys. Res.* 107, <http://dx.doi.org/10.1029/2001JB000355>.
- Schmid, C., Goes, S., van der Lee, S., Giardini, D., 2002. Fate of the Cenozoic Farallon slab from a comparison of kinematic thermal modeling with tomographic images. *Earth Planet. Sci. Lett.* 204, 17–32.
- Segal, A., Praagman, N., 2005. The SEPRAN FEM package. Technical report. Delft Univ. Technol., Ingenieursbureau SEPRAN, The Netherlands, <http://ta.twi.tudelft.nl/sepran/sepran.html>.
- Stegman, D.R., Farrington, R., Capitanio, F.A., Schellart, W.P., 2010. A regime diagram for subduction styles from 3-D numerical models of free subduction. *Tectonophysics* 483, 29–45.
- Steinbach, V., Yuen, D.A., 1995. The effects of temperature dependent viscosity on mantle convection with two mantle major phase transitions. *Phys. Earth Planet. Inter.* 90, 13–36.
- Torii, Y., Yoshioka, S., 2007. Physical conditions producing slab stagnation: Constraints of the Clapeyron slope, mantle viscosity, trench retreat, and dip angles. *Tectonophysics* 445, 200–209.
- van den Berg, A.P., van Keken, P.E., Yuen, D.A., 1993. The effects of a composite non-Newtonian and Newtonian rheology on mantle convection. *Geophys. J. Int.* 115, 62–78.
- van der Meer, D.G., Spakman, W., van Hinsbergen, D.J.J., Amaru, M.L., Torsvik, T.H., 2010. Towards absolute plate motions constrained by lower-mantle slab remnants. *Nat. Geosci.* 3, 36–40.
- van Hunen, J., van den Berg, A.P., Vlaar, N.J., 2002. On the role of subducting oceanic plateaus in the development of shallow flat subduction. *Tectonophysics* 352, 317–333.
- Wada, I., Wang, K., 2009. Common depth of slab-mantle decoupling: Reconciling diversity and uniformity of subduction zones. *Geochem. Geophys. Geosyst.* 10, <http://dx.doi.org/10.1029/2009GC002570>, Q10009.
- Yamato, P., Husson, L., Braun, J., Loiselet, C., Thieulot, C., 2009. Influence of surrounding plates on 3D subduction dynamics. *Geophys. Res. Lett.* 36, <http://dx.doi.org/10.1029/2008GL036942>, L07303.
- Yanagisawa, T., Yamagishi, Y., Hamano, Y., Stegman, D.R., 2010. Mechanism for generating stagnant slabs in 3-D spherical mantle convection models at Earth-like conditions. *Phys. Earth Planet. Inter.* 183, 342–352.
- Yoshioka, S., Naganoda, A., 2010. Effects of trench migration on fall of stagnant slabs into the lower mantle. *Phys. Earth Planet. Inter.* 183, 321–329.
- Zhang, Y., Wang, Y., Wu, Y., Bina, C., Jin, Z., Dong, S., 2013. Phase transitions of harzburgite and buckled slab under eastern China. *Geochem. Geophys. Geosyst.* 14, 1182–1199, <http://dx.doi.org/10.1002/ggge.20069>.